The Origin of Severe Winds in a Tornadic Bow-Echo Storm over Northern Switzerland

WILLI SCHMID AND HANS-HEINRICH SCHIESSER

Atmospheric Science, Swiss Federal Institute of Technology, ETH, Zurich, Switzerland

MARKUS FURGER

Paul Scherrer Institute, Villigen, Switzerland

MARIO JENNI

Institute of Geography, University of Bern, Bern, Switzerland

(Manuscript received 3 September 1998, in final form 10 February 1999)

ABSTRACT

A severe bow-echo storm over northern Switzerland is investigated. Wind damage occurred along a track 15 km long and some 100 m wide. Damage data, meteorological data from a ground micronet, and Doppler radar data are analyzed. Volume-scan radar data in the direction of the approaching storm are available every 2.5 min.

The storm reached a weak-evolution mode when the damage occurred. Updraft impulses followed each other in time steps of typically 5 min. The damage track can be attributed to a strong radar-observed vortex of 2–7-km diameter. The vortex developed at a shear line that was formed by the downdraft outflow of an earlier thunderstorm cell. Most of the damage was collocated with the strongest Doppler winds but some of the damage occurred beneath the strongest signature of azimuthal shear. A weak tornado was observed in that shear region.

The two extremes in Doppler velocity, associated with the vortex and referred to as *inflow* and *outflow* velocities, are analyzed separately. Early strengthening of the vortex at 2–4-km altitude was due to an acceleration of inflow velocity, caused by the rising updraft impulses. Subsequent strengthening at low layers (0–2 km) could be related to acceleration of both the inflow and outflow velocities. At this stage, the diameter of the vortex decreased from about 7 to less than 2 km. The low-level intensification of the vortex is attributed to vortex stretching. Later on, the vortex and inflow velocity at low layers weakened but the outflow velocity remained strong.

1. Introduction

A large mesoscale convective system (MCS) passed over northern Switzerland and southern Germany on 22 July 1995. Hail, water, and wind damage were reported in both countries. The southern part of the system developed into an intense bow-echo, which produced a track of severe wind damage and a weak tornadic event. The parent thunderstorm crossed a dense ground micronet and was captured with a Doppler radar, producing sector volume scans in time steps of 2.5 min. Detailed information about the damage is available. The damage track can be associated with a rapidly growing thunderstorm cell and with a vortex, observed with the radar at low layers.

Bow-echo storms have been investigated in the United States in the last decades. Fujita (1978) defined a bow-echo as an outward bulge within a line of radar echoes and associated the signature with downbursts. He pointed out that the strongest downbursts may occur near the apex of the bow-echo. Two explanations for the formation of a bow-echo exist. A bow-echo can be associated with a rear-inflow jet, caused by entraining of dry air into the rear flank of the storm (e.g., Smull and Houze 1987). Another explanation is that the bow-echo evolves from a redistribution of hydrometeors due to a vorticity couplet circulation (Lee et al. 1992). Such a circulation distorts an elongated radar echo into a bow shape. Przybylinski (1995) showed that bow-echo storms exhibit a variety of features that can be associated either with downbursts, severe straight-line winds, or tornadoes. Multiple vortex circulations within bow-echo storms are documented by Funk et al. (1996a,b). The first of the two studies shows that the vortices developed in the low levels as a cyclonic-convergent zone along the bow apex and intensified and deepened into the middle levels of the storm. The second study discusses such

Corresponding author address: Dr. Willi Schmid, Institute for Atmospheric Science, ETH, CH-8093 Zürich, Switzerland.
E-mail: schmid@atmos.umnw.ethz.ch

© 2000 American Meteorological Society

an evolution in more detail. Three vortex circulations are documented. The three circulations are linked to rapid multicellular growth on the leading convective line. It is argued that vortex stretching is one important element for spinup of the circulations, generally similar to that found by Wakimoto and Wilson (1989).

Studies about European bow-echo storms are rare. Houze et al. (1993) showed that many hailstorms in Switzerland exhibit a ''false hook'' structure, similar to bow-echo storms. Three severe storms in central Switzerland were analyzed in Schmid et al. (1997). Two of the storms had a bow-echo structure. The two storms were similar with respect to the simultaneous occurrence of the strongest wind damage and rapidly growing rotating cells. Another storm with a possible coincidence between a tornado and growing cells has been analyzed by Martin et al. (1997). Hence, these European storms may have similarities to the U.S. storms analyzed by Funk et al. (1996a,b).

Thus, rapidly growing convective cells along a bow-echo are often a source for severe winds, for example, downbursts or microbursts, but also for tornadoes. The link between the growing cells and the damaging winds, however, is not understood in detail. One reason for this is the difficulty of documenting the full sequence of evolving thunderstorm cells and associated vortex signatures. The radar data used by Funk et al. (1996a,b) and Schmid et al. (1997) have a time resolution of 5–6 min. This time step may lead to errors in the process of identifying and tracking cells that follow each other in time intervals of typically 5 min. Radar measurements with a temporal resolution of 2–3 min or less are required for a reliable analysis of these rapidly changing convective elements. High-resolution Doppler studies of similar phenomena exist and demonstrate the possibility to identify relevant processes in the formation of downbursts or tornadoes (e.g., Kessinger et al. 1988; Wakimoto and Wilson 1989; Lee et al. 1992; Roberts and Wilson 1995; Wakimoto and Atkins 1996). However, the question remains of whether one can extrapolate the findings of these studies to the small-scale features along bow-echoes.

The availability of radar volume scans every 2.5 min makes it possible for us to investigate, for the first time, the full cycle of the events that led to the damaging winds. An overview of the available data can be found in section 2. In section 3, we summarize the mesometeorological setting and the evolution of the storm system. The damage and the radar patterns associated with the damage area are shown in section 4. The connection between the damage and the radar-observed vortex is emphasized. In section 5 we investigate the formation and evolution of the vortex. We show how the gust front outflow of an earlier cell triggered secondary cellular growth. A sequence of convective ''impulses'' is observed and analyzed. A simple method is used to demonstrate the link between the growing impulses and the formation of the vortex, and to judge the role of vortex stretching in the subsequent strenghtening of the vortex at low layers. Conclusions are given in section 6.

2. Data and procedures

Meteorological data are available from several data sources: two networks of surface stations, two radiosounding stations, damage data, satellite data, data from the operational radar network of Switzerland, and data from the Doppler radar at the Swiss Federal Institute of Technology (ETH). An overview of the investigated area is given in Fig. 1. The radar station on Albis and the sounding station in Payerne are operated by the Swiss Meteorological Institute (SMI). The Paul Scherrer Institute (PSI) operated a dense network of 12-m towers, measuring wind, temperature, and humidity. Twenty stations were distributed in an area of about 20-km radius (crosses in Fig. 1). Time-averaged measurements of meteorological parameters are stored in 2.5-min intervals. Data from private station owners and from the ANETZ, an automatic network operated by the SMI (stars in Fig. 1) are included in the database. These stations provide additional data of pressure, wind, maximum wind gusts, and precipitation with a time resolution of 10 min.

Satellite data (Meteosat) and the data of the operational C-band radar network are used to document the evolution of the system on the mesoscale (see section 3). Detailed radar measurements of the event were obtained with the C-band Doppler radar at ETH (Li et al. 1995). The radar, which is at 600 m above mean sea level (MSL), operates at a frequency of 5.63 GHz and has a transmitted power of 250 kW, a half-power beamwidth of 1.65°, pulse repetition frequencies (PRFs) of 1200/800 Hz (dual-PRF mode, see, e.g., Keeler and Passarelli 1990), and a pulse width of 0.5 μs. On 22 July 1995, sector volume scans were made between 1443 and 1531 UTC in time steps of 2.5 min. Two volume scans were missed (at 1446 and 1521 UTC). The sector boundaries were continuously adapted such that the storm center was scanned by the radar. The elevation angles were fixed by an automated procedure. The scans were made ''from top to bottom.'' The number of scans per volume decreased from 15 to 9, depending on the distance of the approaching storm from the radar. Two full PPIs at low elevation angles (3° and 20°) were repeated in time steps of 10 min. The collected data were processed following the steps given in the appendix. Hereafter, Doppler velocities toward (away from) the radar are defined as positive (negative) since the storm occurred in direction west–westnorthwest from the radar. In such a setting, the Doppler winds represent roughly the easterly component of the wind vectors.

3. Mesometeorological setting and storm evolution

This section summarizes information about the meteorological environment of the storm and highlights the evolution of the storm system. A surface cold front

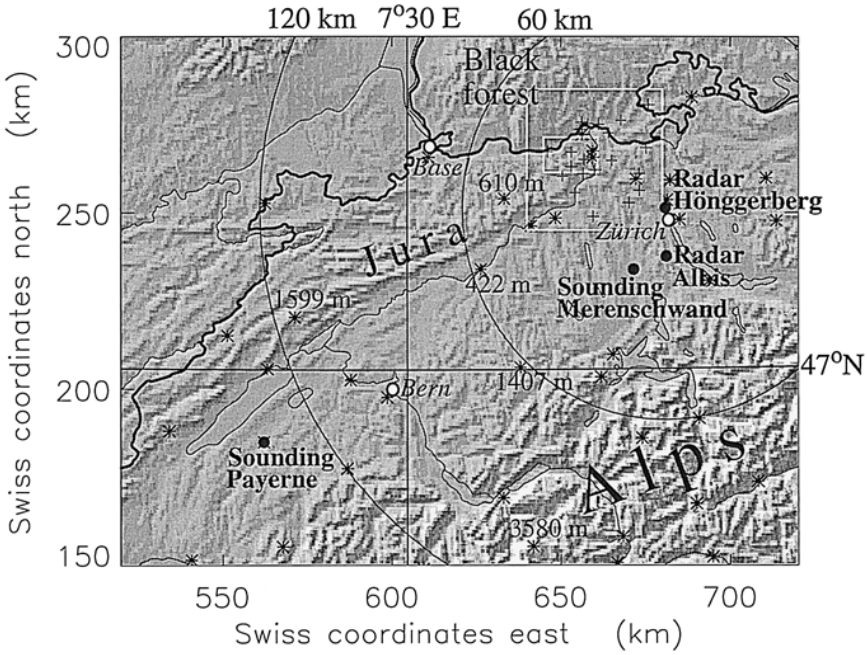

FIG. 1. Overview of the study area. Orography is shown as a relief. Major mountain chains are labeled. Thick solid lines are political boundaries. Thin solid lines are rivers and lakes. Labeled dots mark radar and sounding stations. Labeled small circles mark major cities. Stars mark mesonet stations operated by the SMI. The altitude (mean sea level) of some stations is indicated. Crosses mark mesonet stations operated by the PSI. The two white rectangles show the areas of Figs. 6 (small rectangle) and 10 (large rectangle). The large circles mark the 60-km and 120-km ranges of the radar at Hönggerberg. The Swiss coordinate system is used here. This system is defined such that the coordinates 600 E, 200 N are in Bern.

was associated with a weak upper-level trough over the British Isles (Fig. 2). At 1200 UTC a region with a flat surface pressure distribution over central Europe (Fig. 2b) was located southeast of the front. The front approached from the northwest. A convergence line (dashed line in Fig. 2b) was located about 100 km ahead of the front. This convergence line helped initiate the deep convection that was observed in the subsequent hours.

On the mesoscale, there was a distinct boundary between a moist air mass in the north of Switzerland and a drier one farther southwest. This becomes evident from the ground data (not shown) and from radiosoundings (Fig. 3a) released in Payerne (1200 UTC) and Merenschwand (1400 UTC). The sounding from Merenschwand probably represents best the prestorm thermodynamic environment. The sounding shows a moist layer up to about 600 hPa and a dry layer aloft. An inversion at 800 hPa inhibits the release of convection ahead of the strong frontal forcing.

The Merenschwand sounding did not measure wind. Profiles of horizontal wind were obtained with the volume velocity processing (VVP) technique (Waldteufel and Corbin 1979; Siggia 1991) from the Doppler data of the ETH radar. The VVP technique calculates mean wind vectors from the radial velocities and corrects errors introduced by folded velocity data. Clear-air echoes up to a height of 3-km MSL were visible ahead of the approaching storm. These echoes indicate a substantial change of low-level wind, compared to the wind profile measured with the Payerne sounding. Figure 3b shows the wind hodograph based on a composite of the Payerne sounding and the VVP wind measurements. No VVP wind information is available for the levels above 3 km MSL. It is therefore assumed that the Payerne sounding represents the wind environment of the storm at high altitudes (above 6 km MSL). A linear interpolation of wind was performed for 3–6 km.

The convective available potential energy (CAPE; for definition see Weisman and Klemp 1984), the bulk Richardson number (BRN; for definition see Weisman and Klemp 1984), the bulk Richardson number shear (BRNSHR; for definition see Stensrud et al. 1997), and storm-relative environmental helicity (SREH; see Droegemeier et al. 1993) were calculated from the data shown in Fig. 3. We obtain CAPE = 890 J kg^{-1}, BRN = 18, BRNSHR = 49 m^2 s^{-2}, and SREH = 171 m^2 s^{-2}. These values indicate an environment that represents some intermediary state between tornadic supercell storms and outflow-dominated storms (Stensrud et al. 1997, see, e.g., Fig. 1b in that study). Outflow-dominated storms might be either high-precipitation supercell storms, well-organized MCSs, bow-echo storms, or a combination of these storm types. The environmental

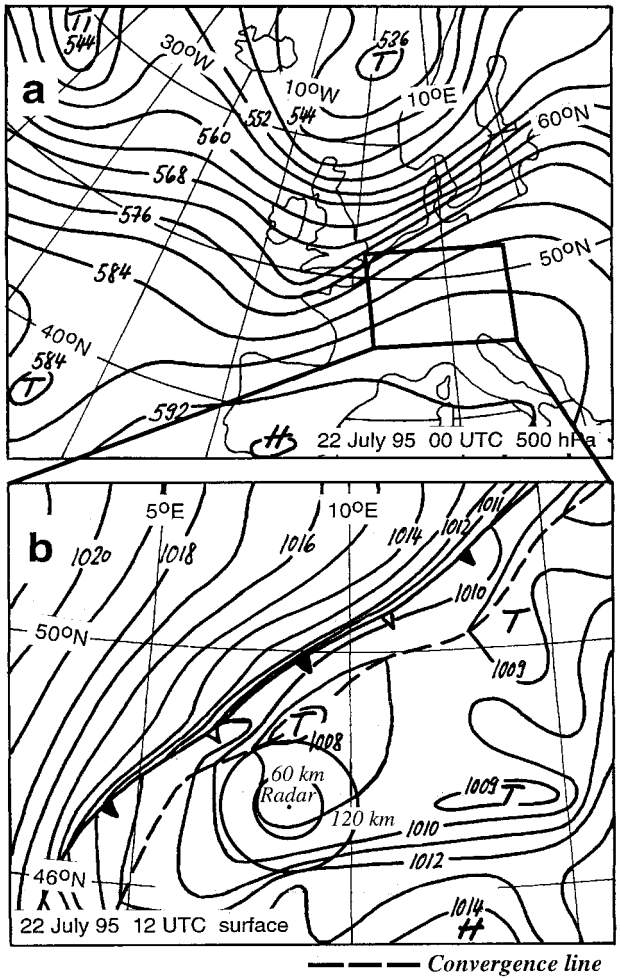

FIG. 2. (a) 500-hPa weather chart and (b) enlarged section of the surface chart for central Europe. Adapted from ''Berliner Wetterkarte.'' The radar at Hönggerberg is shown in (b), together with the radar ranges 60 km and 120 km.

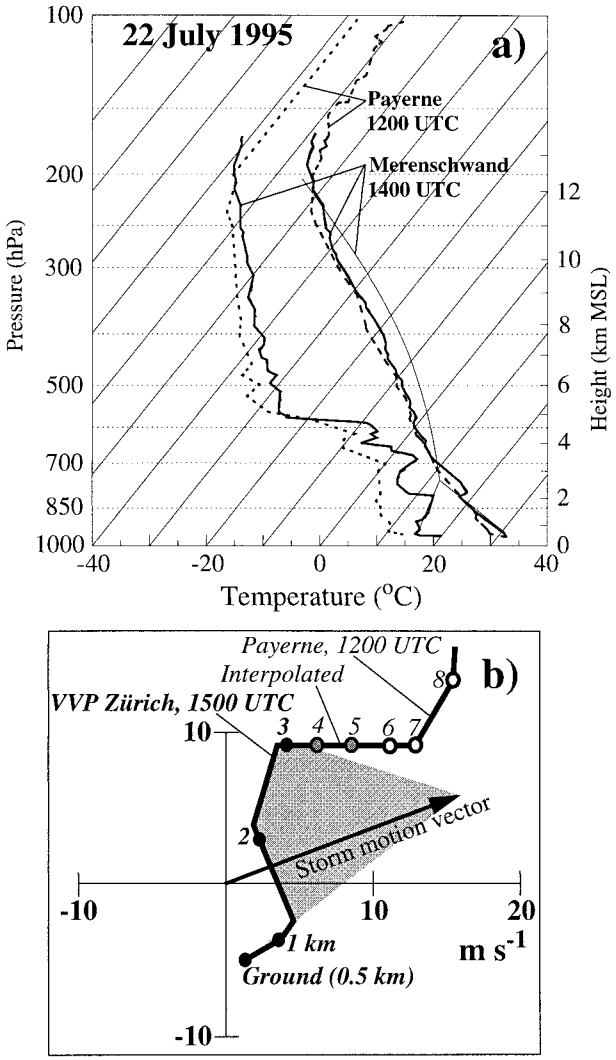

FIG. 3. (a) Two radiosoundings and (b) a composite wind hodograph obtained on 22 July 1995. The numbers in (b) indicate height in km MSL. The arrow in (b) represents the mean motion (250°, 17 m s^{-1}) of two large cells shown in Fig. 11. The shaded area represents storm-relative helicity over a layer from the ground (0.5 km MSL) to 3.5 km MSL.

CAPE for such storms is typically of the order of 1500–3000 J kg^{-1} in the central United States (e.g., Weisman 1993). The CAPE for the here-analyzed storm is lower. One might therefore argue about the reasons why such a well-organized and long-lived system nevertheless could develop. Two reasons can be offered. One of them is the forcing by frontal circulations, and the second is the interaction of the evolving storm with the complex orography (see next paragraph). Both mechanisms can have a significant impact on the organization of convection within mesoscale convective systems (e.g., Hashem and Biggerstaff 1997; Schiesser et al. 1995).

The satellite image of Fig. 4 shows the large cloud shield of the incoming cold front over France and Germany. The convective activity was along the southeastern flank of the cloud system. A cell (arrow, Fig. 4) developed over the ridge of the Jura and grew within 80 min into a large bow-echo storm. At 1430 UTC the cell merged with the incoming storm system, and its leading edge advanced quickly through the orographic gap between Jura and Black Forest (Fig. 5a). This rapid movement produced a bulge toward the southeast. The potentially cold air in the rear of the MCS advanced faster than to the north and south where the line was retarded along the mountains. At 1520 UTC, the severe wind damage and tornado development occurred. A strong bow-echo and large notch in the rear of that part of the system indicate a rear inflow of cold air, according to the conceptual model of a leading line/trailing stratiform (ll/ts) MCS of Houze et al. (1990). The notch might be exaggerated by attenuation of the radar beam by strong precipitation. The cold air moved into the Swiss ''Mittelland'' (enclosed by Jura and Alps) and

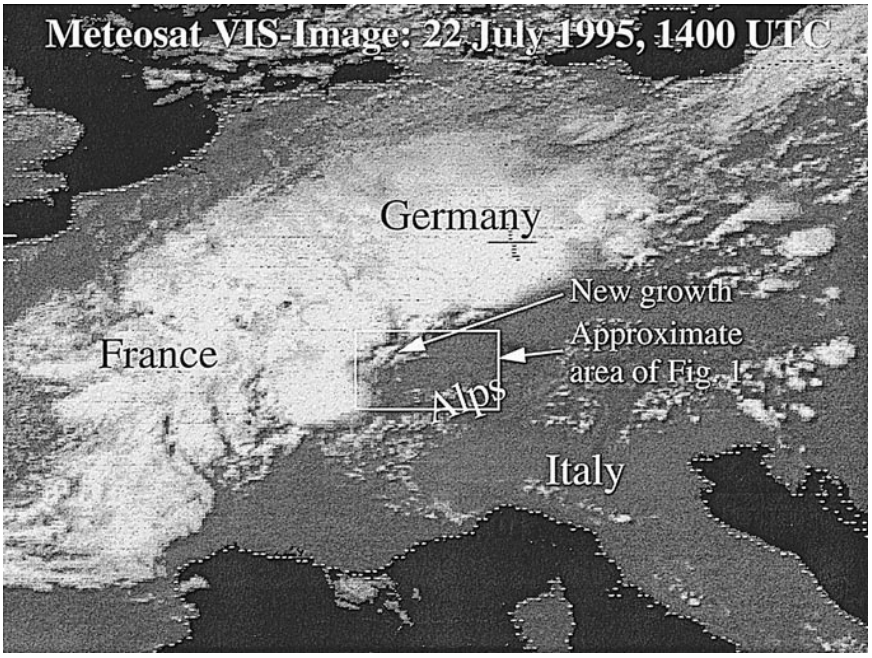

FIG. 4. Satellite image of central Europe (Meteosat, visible), taken on 22 July 1995 at 1400 UTC.

triggered new cells in the warm and moist air. The cells then merged with the advancing MCS.

After 1520 UTC the continuous line grew in length until 1700 UTC when the ideal stage of MCS organization was reached (length of the continuous line about 200 km, total length of broken line at least 260 km, delimited by the edge of the SMI radar image, Fig. 5b). At 1700 UTC, the MCS had a structure almost identical to the archetypical asymmetric ll/ts structure (Houze et al. 1990). This degree of mesoscale organization has not been observed previously in Swiss thunderstorms, at least it was not seen in the entire 5-yr radar-echo climatology of Schiesser et al. (1995). The maximum dimension of the system in north–south direction (derived from composite images of the German and Swiss radars) was about 700 km, and the maximum length of the convective line was about 500 km. These dimensions are larger than the sizes of all other known cases of the recent years in central Europe (Schiesser et al. 1996).

4. Ground observations and low-level radar data

a. Damage information

In the following we focus on that part of the storm that produced the severe wind damage in northern Switzerland. Severe damage occurred in forests and villages along a track about 15 km long and some 100 m wide. A first inspection of the damage was obtained in the weeks after the event. A systematic survey was realized with a delay of almost 9 months, when most of the damage was either already repaired (buildings) or removed (broken trees). While forest clearings were still visible at that time, details like directions of fallen trees could no longer be documented. Damage to buildings was analyzed considering information from local newspapers and from the building insurance agencies. Interviews of people were complemented by inquiries with a survey form. This form was sent to all foresters in the communities that had reported damage. The data were integrated into a geographical information system, and damage maps were produced (Jenni 1997).

The damage region is hilly and is composed of a mix of forests, cultivated land (grass and crops), and small villages. Crop damage is documented by the Swiss hail insurance company but is not considered here. The reason is the difficulty of identifying the source of the crop damage (hail or wind). As a consequence, the damage patterns were not contiguous but occurred in patches with intermediary areas without documented destruction (Fig. 6). Forest damage included single broken trees in otherwise undestroyed areas, small groups of broken or uprooted trees, and complete clearings with widths of the order of 100 m. Many trees were broken at half height (6–10 m above ground), some of them showing effects of rotating winds. The patterns of the uprooted or broken trees mostly showed diverging airflow except for one spot where the fallen stems were oriented in all directions. A total volume of 15 000 m^3 wood in trees was felled by the storm. Damage to buildings consisted mostly of destroyed or removed roofs and tiles. Repair costs exceeded two million Swiss francs (about 1.5 million U.S. dollars). Buildings outside the main damage track remained almost untouched.

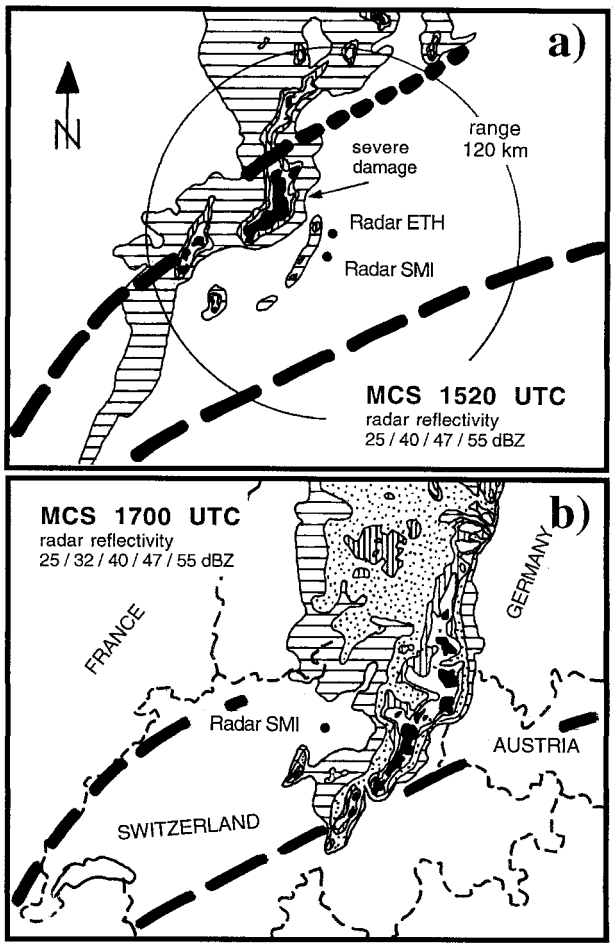

FIG. 5. The evolving MCS, seen with the radars of the SMI, at (a) 1520 UTC and (b) 1700 UTC. The thick dashed lines indicate major mountain chains (the Alps in the south, the Jura in the west, and the Black Forest in the north, cf. Fig. 1).

b. Damage patterns and Doppler radar velocities

Figure 6 shows the locations of the heaviest damage and contours of constant Doppler velocity, observed at the lowest elevation angle. The radar measurements were taken at about 300–500 m above the ground. One notes a good spatial agreement between the locations of the damage and the maximum Doppler winds at Sulz/Leidikon and Mandach. At Oberhofen and Hottwil, the damage occurred a bit north of the strongest Doppler winds and was collocated with large azimuthal shear (1515 and 1517 UTC). The pattern of Doppler velocity indicates a small vortex (diameter about 1 km, azimuthal shear about 3×10^{-2} s^{-1}) at this stage (Fig. 7). The size of the vortex is of the order of the spatial resolution of the radar beam. The vortex was possibly smaller and stronger than seen with the radar, and thus may have reached tornadic strength. The pattern of radar reflectivity shows a hook echo, most probably caused by precipitation particles wrapped around the center of the vortex (Fig. 7).

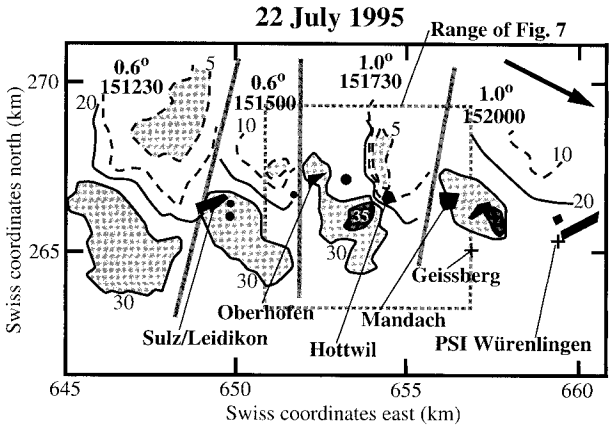

FIG. 6. Map of the damage areas and the associated Doppler velocity patterns, observed at the lowest available elevation angle. Damage areas are black. The names of villages affected by the damage are indicated. Contours of constant Doppler velocity are solid (20, 30, and 35 m s^{-1} toward the radar) and dashed (5 and 10 m s^{-1} toward the radar). These contours were drawn from unsmoothed plots of Doppler velocity. The Doppler patterns observed at different times are separated by gray-shaded bars. The times (UTC) and the elevation angles of the associated radar scans are also indicated. The crosses mark the locations of two meteorological ground stations mentioned in the text. The arrow in the upper-right corner of the figure shows the direction toward the radar. The square (dotted, gray shaded) marks the range of Fig. 7.

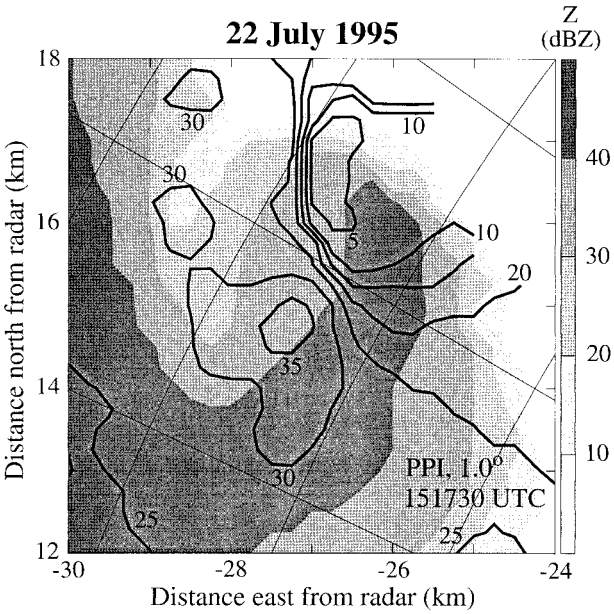

FIG. 7. Reflectivity (gray shaded) and Doppler velocity (solid lines) of the vortex signature, observed on 22 July 1995, 1517 UTC, at the lowest available elevation angle. A three-point median smoother was applied to the arrays of reflectivity and Doppler velocity. Radar range circles and azimuth lines are drawn in steps of 2 km and 5°, respectively.

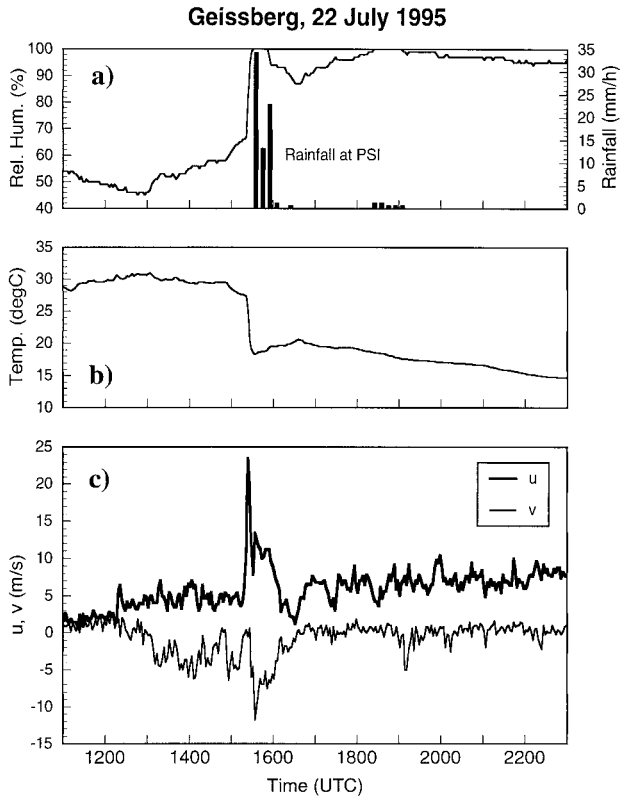

FIG. 8. Time series of (a) relative humidity at the station Geissberg and rainfall rate at PSI, (b) temperature at Geissberg, and (c) the u and v components of wind at Geissberg. Two and one-half–minute averages are shown. Rainfall values at PSI are 10-min averages. The locations of Geissberg and PSI are shown in Fig. 6.

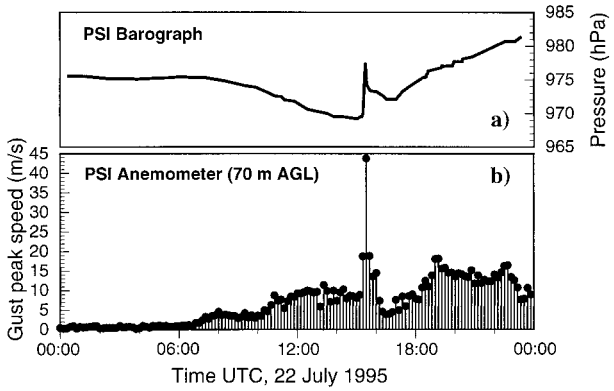

FIG. 9. (a) Pressure and (b) gust speeds measured at PSI (location see Fig. 6). The pressure trace was manually extracted from a microbarograph paper strip. Due to a systematic drift of the instrument clock, the data have been shifted by about 20 min to coincide with the peak in wind speed.

c. *Eyewitness reports*

A 10-year-old boy from Oberhofen (damage location see Fig. 6) observed a tornado funnel close to his home. He stated that the funnel was over a corn field for some time, whirling crop debris around its center. The funnel was transparent, with a diameter of a couple of meters. Visibility was good, that is, more than 500 m. Another eyewitness in the village of Mandach reported heavy precipitation and a visibility of 10 m (''white wall''). In this case a tornado funnel was not explicitly observed.

d. *Meteorological surface data*

Precipitation, partly hail, was short in duration and mainly collocated with the convergence line. Ten-minute averages of rainfall intensity varied between 4 and 34 mm per hour (Fig. 8a). Temperature (Fig. 8b) dropped by about 10°–12°C during the passage of the storm. Wind speeds showed mostly a narrow maximum at the same time, in some cases together with a shift of wind direction toward northwest and north (Fig. 8c, see also Furger et al. 1996). However, a wind shift did not occur at stations lying in valleys oriented parallel to the airflow. The station Geissberg recorded a peak value of 23.4 m s^{-1} (2.5 min average) at 12 m above ground level (AGL; Fig. 8c). During the subsequent hour, winds faded to almost calm, and at some stations easterly flow occurred for a while.

The pressure trace of a conventional microbarograph at PSI showed an almost instantaneous pressure increase of 8.5 hPa and a subsequent drop of 4 hPa within a few minutes (Fig. 9a). The exact duration of the pressure peak cannot be determined from the barograph strip. The ANETZ station at PSI measured a peak gust speed (10-s average) of 43.8 m s^{-1} between 1520 and 1530 UTC (Fig. 9b) with an anemometer mounted on a stack, at 74 m AGL.

A synoptic representation of the isochrones of wind speed maxima measured with PSI's network reveals the movement of an organized structure from west to east with speeds between 11 and 33 m s^{-1} (Fig. 10). The variation of the spacing between isochrones is a signature of varying propagation velocities and must be attributed partly to frictional effects of the topography, and partly to the dynamics of the storm itself. At 1520 UTC a bulge toward southeast can be recognized just west of the city of Brugg. This bulge can be attributed to the deformation of the gust front seen with the radar data (Fig. 11, see section 5a).

e. *Discussion*

Strong winds in a thunderstorm connected to a line of destruction can be attributed to microbursts, tornadoes, or a storm-relative rear-to-front jet (Biggerstaff and Barritt 1996). In an attempt to identify the sources of destruction, we discuss hereafter the observations near Oberhofen and PSI Würenlingen (locations see Fig. 6).

The rotating, but transparent ''whirlwind'' observed near Oberhofen may have been a suction vortex (Fujita 1981) or a tornado funnel not extending visibly to the

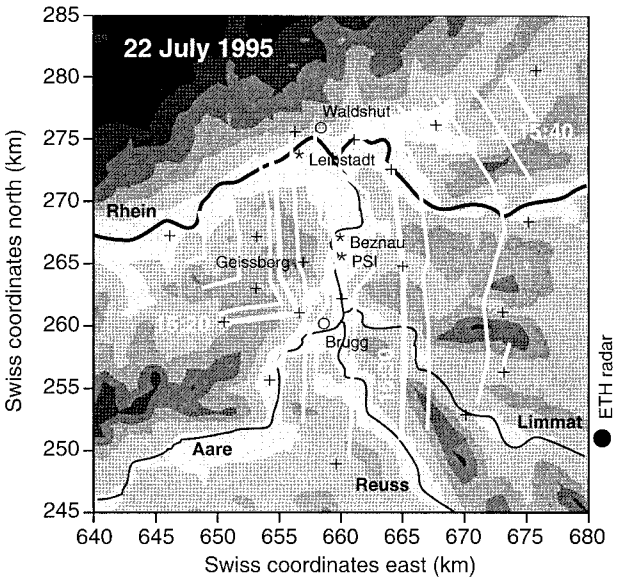

FIG. 10. Isochrones of wind speed maxima (white lines), retrieved with an objective procedure from the data of the ground networks. Black lines are rivers. The height of the ground is gray shaded (300–1000 m MSL, in steps of 100 m). Each ground station of PSI's network is marked with a +. Stars locate ANETZ stations of the SMI. Major cities are marked with circles. The names of some locations and of the rivers (bold) are also given. (Reproduced with the permission of the Swiss Federal Office of Topography, dated 24 July 1998.)

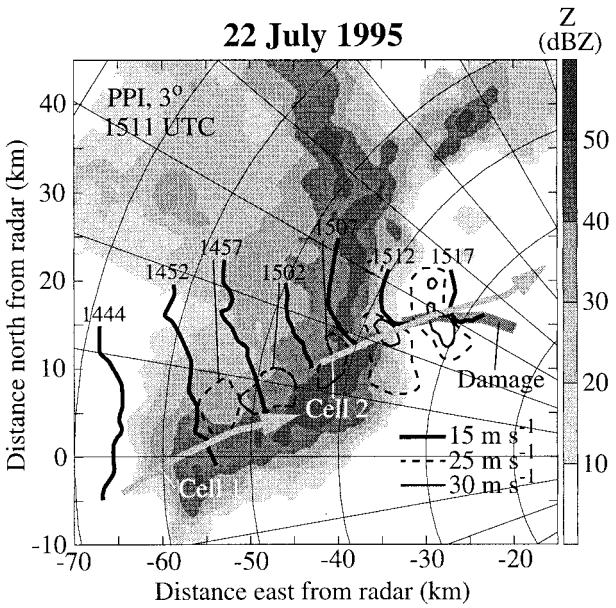

FIG. 11. Reflectivity pattern (gray shaded) at 1511 UTC of the bow-echo. The light arrows mark the paths of two large thunderstorm cells, determined from the reflectivity cores at 8-km altitude. The time periods of the two cells are 1443–1459 UTC (cell 1) and 1506–1531 UTC (cell 2), see also Fig. 12. The gray-shaded line marks the damage track. The solid and dashed black lines are contours of Doppler velocity, seen from the sector-volume radar scans at the lowest available elevation angles. The contour lines are truncated at the boundaries of the sector-volume scans. Radar range circles and azimuth lines are drawn in steps of 10 km and 10°, respectively.

ground. This is not uncommon in mountainous terrain, probably due to drier environments at lower levels (Bluestein and Golden 1993; Szoke et al. 1984). Lack of other visual observations must be attributed partly to obstructed viewing in hilly orography, and partly to the absence of well-trained observers. People in Switzerland do not know how to watch thunderstorms, and tornado chasing is almost unknown. The eyewitness observation is consistent with the radar patterns. The largest azimuthal shear occurred over the locations of Oberhofen and Hottwil (Fig. 6). The formation of a damaging tornado was therefore most probable in that region.

Farther east, the shear signature weakened rapidly but the maximum Doppler velocities remained strong (Fig. 6). Therefore, the damage near Mandach and PSI/Würenlingen was most probably caused by nontornadic winds. This interpretation of the Doppler signatures is in good agreement with the ground observations. The barograph at PSI (Fig. 9a) did not register any extraordinary pressure drop that could indicate the vicinity of a tornado. Pressure drops up to 5 hPa have been observed within a radius of less than 1 km from the funnel of a tornado (Bluestein and Golden 1993). We conclude that no tornado was closer than 1 km to the PSI area. This is consistent with the damage survey in the forest of Würenlingen, where the area with the heaviest destruction was located roughly 1 km north of PSI (location see Fig. 6). In this place, at a particular spot, stems from uprooted and broken trees were pointing in any direction, although most of the fallen trees in the surroundings were streamlined in a west–east direction. No rotational structure could be determined. In such a setting, one or two microbursts could cause the observed pattern of the fallen trees. Damage to a cornfield resembling the patterns of deflected microbursts was observed and photographed nearby from a motorglider (Fuchs 1998, personal communication). Another spot immediately to the east of PSI showed a more organized pattern of fallen trees, as expected from a microburst.

The pressure variations in Fig. 9a at about 1520 UTC can be interpreted in terms of a possible microburst that is embedded within the gust front head of a cold air outflow. The signature is similar to, but more distinct than the signatures typically associated with a pure gust front (Charba 1974; Johnson and Hamilton 1988). After the jump, the pressure remained 4 hPa higher, indicating the mesohigh (Johnson and Hamilton 1988). At about 1700 UTC the wake depression caused a local pressure minimum that preceded a steady, postfrontal pressure rise. The PSI anemometer (Fig. 9b) registered extreme wind gusts within one single 10-min time interval. However, considerable gustiness also occurred in the immediately preceding and following time intervals. Hence, the overall duration of strong gustiness was at least 10 min, or more than twice as long as expected for a pure microburst (Fujita 1985).

In summary, a combination of a short-lived tornado and several microbursts embedded in a larger rear-to-front jet gives the most consistent interpretation of the observations. Tornadoes and microbursts occurring in close vicinity are not uncommon, see, for example, Forbes and Wakimoto (1983). From the damage assessment the event could be classified as F1 or F2 on the Fujita scale (Fujita 1981), which is consistent with the peak gust speed measured at PSI. Such a classification is subject to uncertainties. In hilly terrain, local confluence and diffluence of air may contribute to a strengthening or weakening of wind. It is probably impossible to assess the local effects of hilly orography on heavy wind in the here-analyzed case.

5. Radar history

a. Gust front

Section 3 showed that the parent thunderstorm was part of a large and well-organized MCS that produced a bow-echo in the region where the vortex occurred (Fig. 5a). The bow-echo is enlarged in Fig. 11. The vortex developed near the apex of the bow, at about 40 km west and 15 km north of the radar (Fig. 11). An analysis of the volume radar data revealed that two strong thunderstorm cells (cell 1 and cell 2 hereafter) occurred during the period of interest. The two cells dominated many smaller and short-lived cells. The tracks of the two cells are indicated in Fig. 11, together with the damage track. Both cells were triggered by a gust front that originated from former thunderstorm cells. The gust front can be seen in the patterns of Doppler velocity, observed with the lowest sector-volume scans. Figure 11 shows the contours of 15, 25, and 30 m s^{-1} Doppler velocity in time steps of 5 min. The contour 15 m s^{-1} is an indicator for the position of the gust front since this contour corresponds with maximum convergence. It turns out that the gust front propagated mainly from west-southwest to east-northeast. The gust front was originally oriented along a more or less straight line. A deformation becomes apparent at about 1507 UTC. The maximum Doppler velocity increased and reached peak values of about 35 m s^{-1} 10 min later.

Figure 12a shows a time–height diagram of maximum radar reflectivity, derived from horizontal radar cross sections (CAPPIs), for cell 1 (1443–1459 UTC) and cell 2 (1506–1531 UTC), respectively. Only reflectivities larger than 44 dB*Z* are shown. This diagram does not cover the whole life cycles of the cells. For clarity, cell 1 is shown up to 1459 UTC only although the cell survived this time by a couple of minutes. Cell 2 was captured at the time when the 55-dB*Z* contour was first identifiable as a separate entity. The formation of cell 2 is collocated with the formation of the vortex, also shown in Fig. 12a. The vertical extension of the vortex was determined by a careful inspection of the patterns of Doppler velocity and azimuthal shear. The data of

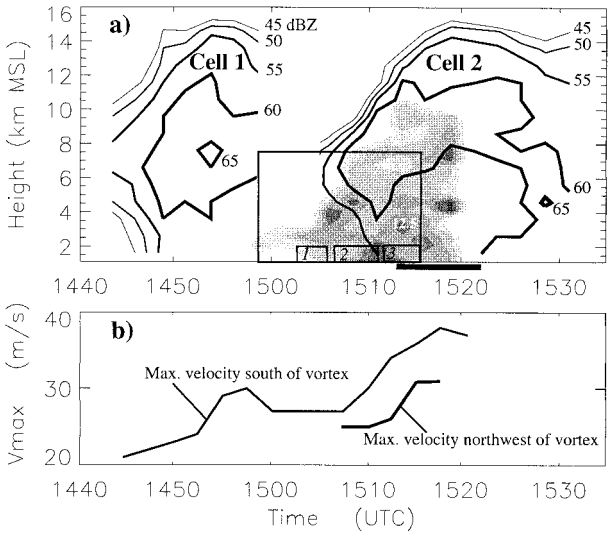

FIG. 12. Time evolution of some radar parameters. Maximum reflectivities of cells 1 and 2 are shown in (a). Azimuthal shear of the vortex is gray shaded in steps of 2.5×10^{-3} s^{-1} and starts at 5×10^{-3} s^{-1}. The white numbers indicate azimuthal shear (in units of 10^{-3} s^{-1}). The solid bar marks the time when the vortex passed the damage region. The large rectangle marks the range of Fig. 15. The labeled small rectangles refer to specific stages in the evolution of the vortex (for details see text). (b) The time evolution of maximum Dopper velocity (northwest and south of the vortex). These values were derived from the radar data at the lowest available altitude (1.1 km MSL).

azimuthal shear were smoothed with a seven-point median smoother. The signatures of maximum azimuthal shear were identified at various altitudes, and the signatures were attributed to the same vortex when the axis through the centers of the signatures was tilted by less than 45° from the vertical. The formation and evolution of the vortex are discussed in section 5c. The vortex remained within the analysis domain up to 1520 UTC. After that time, the vortex left the domain of the sector-volume scans. Therefore, the analysis of the vortex is restricted to the time period before 1520 UTC.

The maximum Doppler velocity behind the gust front is a measure for the strength of the gust front outflow since the viewing angle of the radar coincides within some 10° with the direction of the gust front outflow. The time evolution of maximum Doppler velocity, observed at 1.1 km MSL, is plotted in Fig. 12b. The figure shows that the outflow is accelerated during two specific periods: 1453–1458 UTC and 1508–1518 UTC. The origins of this acceleration are not the same for the two periods. To understand the possible source of acceleration for the first period, we show hereafter the patterns of reflectivity and Doppler velocity at 1451 UTC (Fig. 13), that is, immediately before the acceleration of the outflow is observed. The horizontal cross section (Fig. 13a) at 6-km altitude points to a Doppler pattern typical for a splitting thunderstorm (e.g., Klemp 1987). Three signatures of large azimuthal shear (marked with letters A, B, and D in Fig. 13a) indicate rotation. The southern

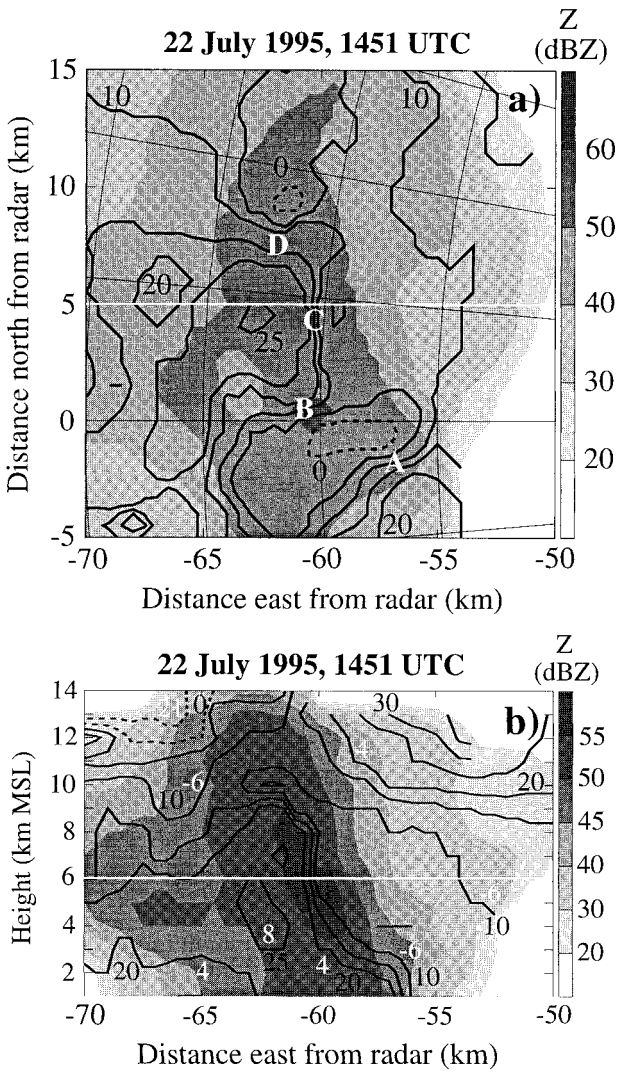

FIG. 13. (a) Horizontal and (b) vertical cross sections through cell 1. Radar range circles and azimuth lines are drawn in (a) in steps of 5 km and 5°, respectively. Reflectivity (gray shaded) and Doppler velocity (solid and dashed lines) are shown. The contours of Doppler velocity are partly labeled with black numbers (ground-relative, m s^{-1}, positive values for motion toward the radar), and partly labeled with white numbers (storm-relative, assuming a storm motion of 16 m s^{-1} toward the radar). The white line in (a) marks the location of the vertical cross section. The white line in (b) marks the altitude of the horizontal cross section. Signatures of large azimuthal and radial shear are labeled with white letters in (a).

signature (A) is probably associated with a cyclonically rotating vortex at the southern edge of the updraft whereas signatures B and D point to vortices associated with the edges of the downdraft. One would also expect a vortex signature to the north of signature D, being associated with a vortex at the northern edge of the updraft. This signature does not appear, most probably because the updraft was nonexistent or weak in that region. In fact, the divergence pattern at high levels (not shown) indicates that the strongest updraft is located in the vicinity of vortex signature A.

Signature C (Fig. 13a) indicates convergence at the boundary between updraft and downdraft. This convergence is visible through a deep layer of 9 km (Fig. 13b). Midaltitude convergence is an indicator of a strong downdraft leading to heavy surface winds (Schmocker et al. 1996). Hence, the gust front is most probably accelerated by the downdraft of cell 1. Figure 11 shows the first appearance of the 25 m s^{-1} contour of Doppler velocity at 1457 UTC. This contour moved in direction of east-northeast. The associated enhanced flow contributed to the deformation of the gust front and to the formation of a shear line some minutes later.

b. Updraft impulses

It was already noted that two cells dominated the storm evolution. A refined analysis, however, shows a more complex pattern of convective cells. Following Foote and Frank (1983) we use hereafter the term *updraft impulses* or briefly impulses for those convective units that tend to merge continuously with the main updraft, hence, are not identifiable as individual updrafts. Foote and Frank (1983) defined impulses as local maxima in vertical wind velocity, retrieved from multiple-Doppler data. Here, we use volume-scan data from a single-Doppler radar. It is therefore not possible to retrieve vertical wind. However, single-Doppler data allows examination of the patterns of reflectivity and Doppler velocity in three dimensions, and one can utilize the full resolution of the data. Animations of 3D displays allows for visualization of the evolution of successive impulses. We discuss isosurface plots of reflectivity and vertical cross sections, taken in the west–east direction through the volume-scan data of reflectivity and Doppler velocity. These cross sections reveal patterns that point to the formation and further development of updraft impulses. Several criteria can be used to identify an impulse:

1) A local minimum in Doppler velocity, indicating that the inflow from the east is accelerated.
2) A local maximum of reflectivity or an eastward or upward extension of a high-reflectivity zone, preferably above a zone with lower reflectivity (weak echo region).
3) A signature of convergence, normally located a bit west of the minimum in Doppler velocity and below the reflectivity signature of the impulse.

It was found that these signatures moved upward. The ground-relative motion remained small. This means that the signatures moved into the approaching storm system. For proper identification of the impulses, we used the following procedure. First, local minima of Doppler velocity (criterion 1) were identified in the full-volume data sample. Second, the minima were grouped such

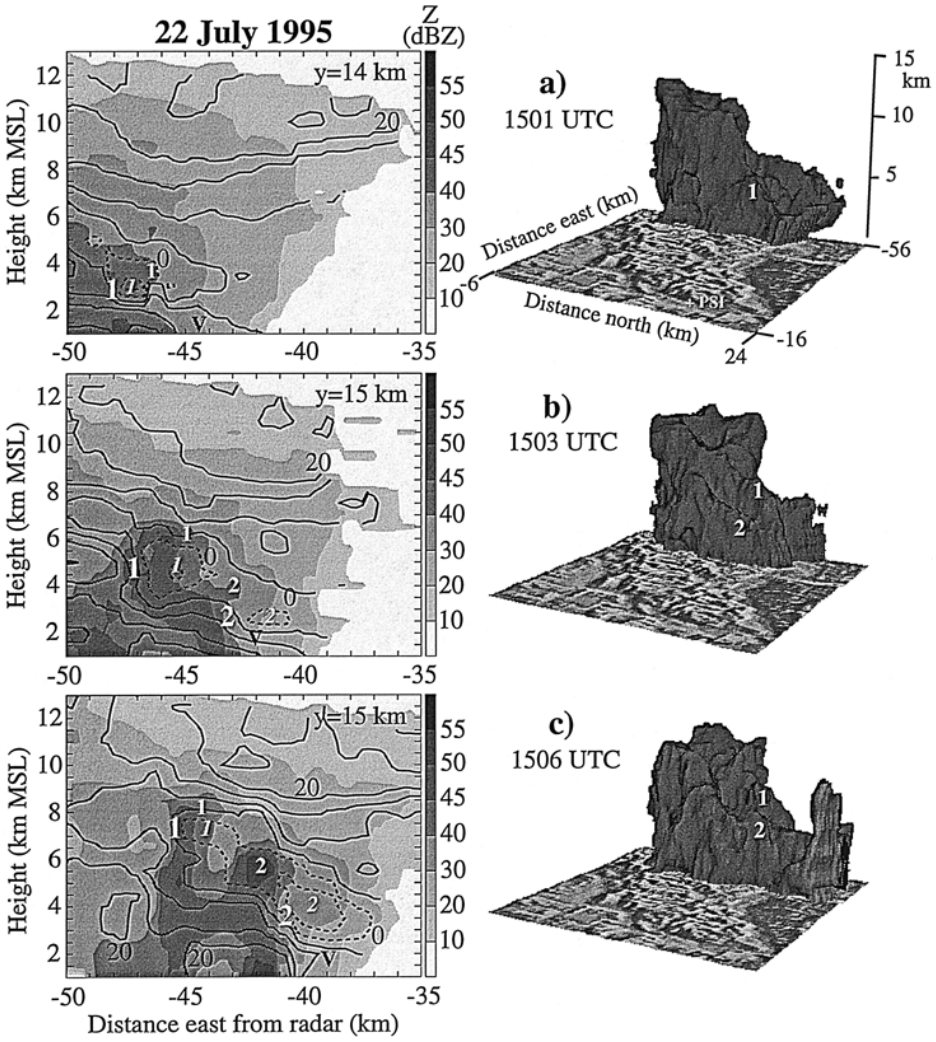

FIG. 14. (left) West–east cross sections of reflectivity and Doppler velocity, and (right) the 40-dB*Z* isosurface, together with a relief of orography. The diagrams (a)–(g) refer to the period 1501–1516 UTC. The location of each cross section is indicated in the upper-right corner of the diagram (y = . . . km north of the radar). Reflectivity (gray shaded) and Doppler velocity (solid and dashed lines, partly labeled

that they represent growing impulses. Third, the fulfillment of criteria 2 and 3 was tested.

Three impulses were identified immediately north of the vortex. The impulses are visualized in Fig. 14 with a sequence of vertical cross sections and with plots of the 40-dB*Z* isosurface, obtained with the ARGOS software (Bresch and Liniger 1998, personnel communication, for details see http://www.lapeth.ethz.ch/argos/). The white numbers refer to the signatures of these impulses. The italic numbers mark the local minima in Doppler velocity. The small roman numbers point to the reflectivity signatures, and the large roman numbers highlight the convergence signatures. Impulse 1 is first seen at 1501 UTC at a height of 3 km (Fig. 14a). A local minimum of Doppler velocity is located immediately east of the convergence signature, and the 40-dB*Z* reflectivity contour shows a small bulge toward the east at location 46.5 km west and at 3.5-km height. Thus, the three defined criteria for an impulse are visible. The impulse is also associated with a signature of horizontal shear (at position −47 km west and at 2-km height). This horizontal shear points to a rotor, located at the boundary between the gust front outflow and the inflow stream. The rising impulse 1 is clearly visible at 1503 and 1506 UTC (Figs. 14b and 14c) and appears to disintegrate later on (Fig. 14d).

Impulse 2 is first visible at 1503 UTC at position 42 km west (Fig. 14b). Again, one notes substantial horizontal shear at the boundary between inflow and gust front outflow. The subsequent rise of the impulse can be followed up to 1513 UTC (Fig. 14f). The impulse became much stronger than impulse 1 and was associated with a weak echo region at 1508 UTC (Fig. 14d). Impulse 2 can be attributed to the formation of cell 2.

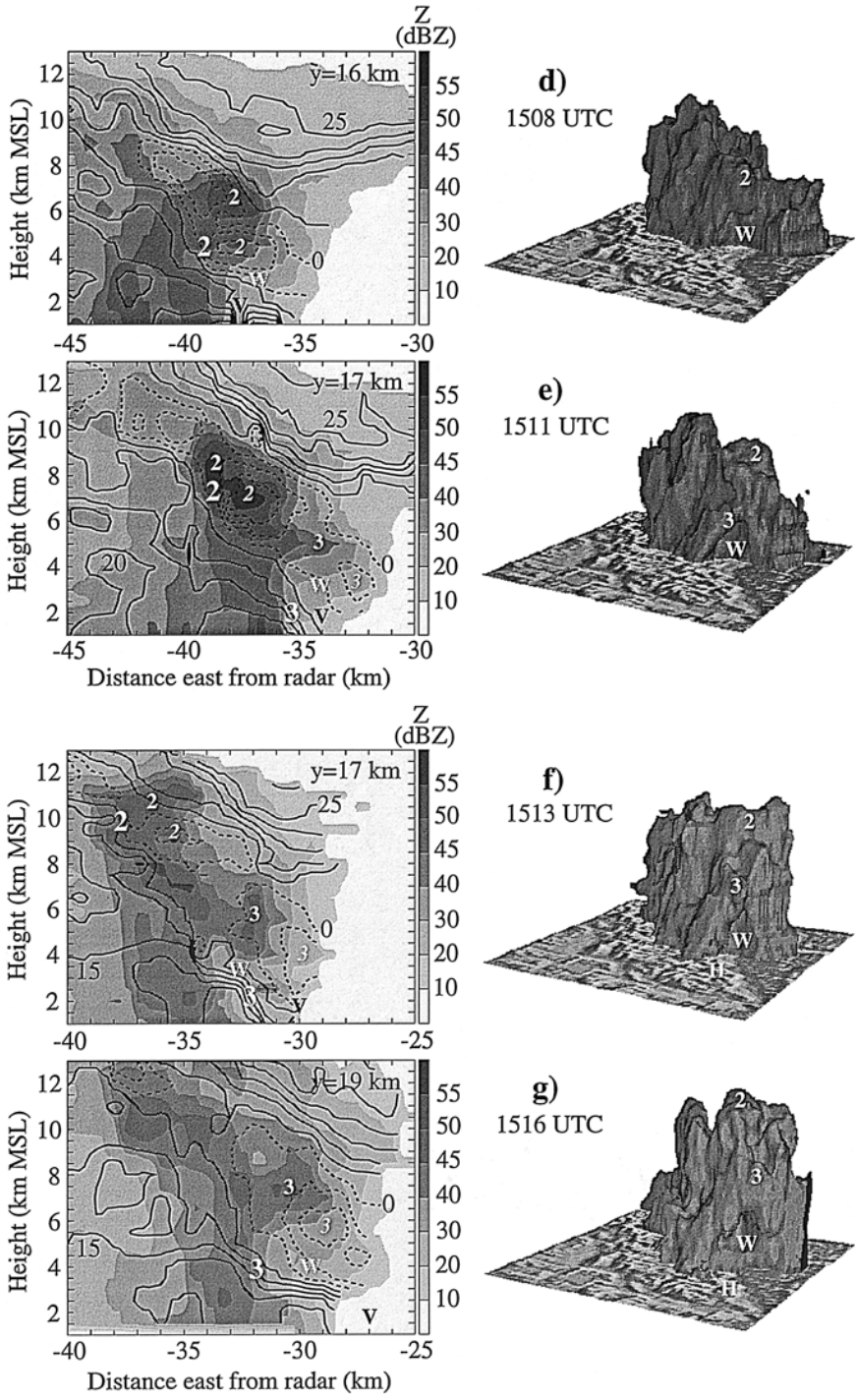

FIG. 14. (*Continued*) with black numbers) are shown. Updraft impulses are highlighted with white numbers (for details see text). The label V marks the *x* coordinate of the vortex center near the ground. The viewing direction to the isosurfaces is from east-northeast. The label W marks a weak echo region, and the label H marks a hook echo, also visible in Fig. 7.

Impulse 3 can be identified first at 1511 UTC and tracked until 1516 UTC (Figs. 14e–g). This impulse evolved above a marked weak echo region.

The analysis shows that the three documented impulses followed each other in time intervals of 3–7 min. The horizontal distance between the core of the impulses is less than 5 km. These scales are smaller than the typical scales of multicell storms (10–20 min and 10–

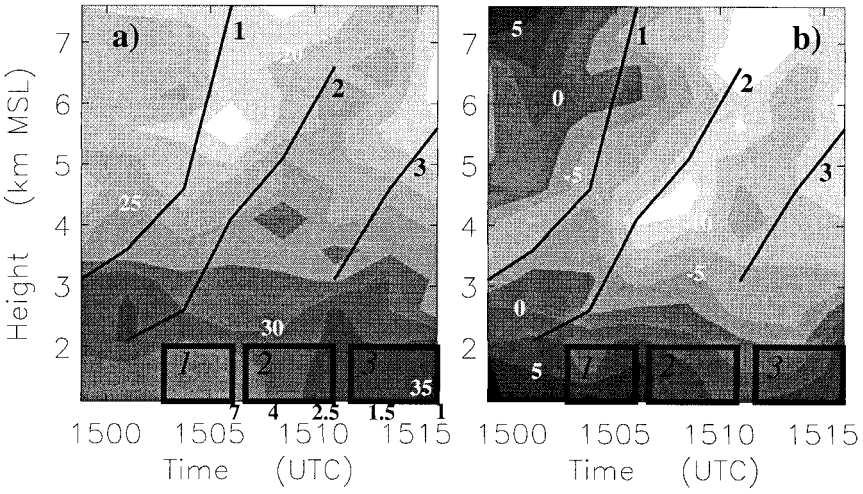

FIG. 15. Shaded contours of (a) maximum Doppler velocity in the outflow region south of the vortex and (b) minimum Doppler velocity in the inflow region north of the vortex. The white numbers mark the velocities of the contours (m s^{-1}). The black lines mark the altitudes of three convective impulses (1, 2, and 3, see section 5b). The labeled rectangles agree with the small rectangles of Fig. 12a and refer to the discussion in section 5c. The numbers at the bottom of (a) indicate the diameter of the vortex (in km) near the ground.

20 km, respectively, see, e.g., Smull and Houze 1985; Fovell and Ogura 1988; Fovell and Dailey 1995). The impulses represent modulations of the overall updraft rather than individual updrafts. The here-analyzed storm therefore reached a *weak-evolution* mode (Foote and Frank 1983) when the damaging wind gusts were formed.

c. Evolution of the vortex

Azimuthal shear is normally used to quantify the strength of a vortex signature and to highlight the evolution in height and time of a vortex (e.g., Vasiloff 1993). Azimuthal shear was calculated from the Doppler velocities and smoothed with a seven-point median smoother (see appendix). The smoothing is necessary to reduce the noise in the data. However, features with a scale less than 3–4 km tend to disappear. Therefore, azimuthal shear is underestimated if the diameter of a vortex is less than 3 km. The diameter of the investigated vortex (i.e., the distance between the extremes in Doppler velocity) is typically 4–5 km. We believe that the smoothing yields a reasonable estimate of azimuthal shear between the extremes in Doppler velocity. One specific period, for which the diameter of the vortex decreased to less than 2 km, is discussed later on.

We also investigate the extremes in Doppler velocity associated with the vortex. Figure 15a shows a time–height diagram of maximum Doppler velocity (retrieved from CAPPIs) south of the vortex center (*outflow velocity* hereafter). Figure 15b shows, in a similar manner, the minimum Doppler velocity north of the vortex center (*inflow velocity* hereafter). First, we point to the change of inflow velocity associated with the rising impulse 2. Figure 15b indicates a substantial acceleration of inflow velocity from 2–4-km altitude. This acceleration can probably be associated with a midlevel low pressure perturbation noted by LeMone (1983) and further discussed by Fovell and Ogura (1988). The acceleration of inflow velocity contributes substantially to the formation and strengthening of the vortex.

Second, we discuss the evolution of the vortex at low altitudes (below 2 km MSL). For this, we distinguish between three stages, indicated with rectangles and italic numbers in Figs. 12a and 15.

Stage 1: An increase of azimuthal shear is seen during stage 1 (Fig. 12a). The key for explanation of this increase can be found in Fig. 11. One notes that the velocity contour 25 m s^{-1} approaches the velocity contour 15 m s^{-1} between 1502 and 1507 UTC. The discussion in section 5a has shown that the velocity contour 25 m s^{-1} can be attributed to the downdraft outflow of cell 1. Hence, it is suggested that this downdraft outflow contributed to the formation of a shear line during stage 1.

Stage 2: One notes for some minutes a symmetric acceleration of both extremes in Doppler velocity (cf. Figs. 15a and 15b). The distance between these extremes decreases significantly (see the numbers at the bottom of Fig. 15a). These changes are probably caused by forces that act simultaneously on both extremes in Doppler velocity. These forces can be associated with a pressure perturbation caused by the updraft impulses 2 and 3. It is probable that a strong updraft existed above the low-level vortex during stage 2. Vortex stretching (e.g., Wakimoto and Wilson 1989) can therefore explain the observed vortex intensification at this time and altitude.

Stage 3: In Fig. 12 one notes a decrease of azimuthal

shear. This decrease is only partly realistic since the diameter between the extremes in Doppler velocity is less than 2 km during that stage (Fig. 15a and Fig. 7). The smoothed azimuthal shear, shown in Fig. 12a, underestimates the azimuthal shear of the low-level vortex at 1513–1517 UTC. However, the vortex weakened rapidly later on, as already noted in section 4e (Fig. 6). A decrease of inflow velocity is responsible for this weakening (Fig. 6) whereas the outflow velocity remained strong. Note that the inflow velocity already started to weaken during stage 3 (Fig. 15b). We assume that the outflow velocity was kept strong by a downdraft. A signature for a possible downdraft can be seen in Figs. 11 and 12b. Figure 11 shows at 1512 and 1517 UTC a secondary maximum in Doppler velocity, some kilometers northwest of the vortex. We traced this maximum in a similar manner as the primary maximum in the south of the vortex center. Figure 12b shows that this maximum is accelerated at about 1515 UTC. This acceleration is not affected by the vortex, hence, it is probably a fairly undisturbed downdraft signature. The presence of a downdraft reaching low levels is probable at that time but it remains an open question how and to what degree such a downdraft interacted with the vortex.

So far, we used multicell/squall line concepts for interpretation of the observations. The analysis, however, has shown that the storm reached a weak-evolution mode. The weak-evolution mode represents an intermediary state between the multicell mode and the supercell mode (Foote and Frank 1983). Therefore, supercell concepts (e.g., Lemon and Doswell 1979; Wicker and Wilhelmson 1995; Dowell and Bluestein 1997) may also be important for a complete interpretation of the observed events. We probably have to await numerical model simulations in order to obtain a more quantitative assessment of the factors that influence the formation of severe winds in the analyzed storm.

6. Conclusions

A large MCS developed on 22 July 1995 over eastern France and propagated eastward over southern Germany and northern Switzerland. The size and the degree of organization was extraordinary for central Europe. A bow-echo formed near the southern edge of the system and could be attributed to a track of severe wind damage. A coherent picture of the events that led to the damaging winds was found:

1) The downdraft of a thunderstorm cell accelerated locally the existing gust front outflow.
2) A bulge in the gust front formed. This bulge led to a shear line and to heavy secondary convection.
3) The storm reached a weak-evolution mode. Several updraft impulses developed within 15 min. The inflow wind of the rising impulses accelerated at layers 2–4 km MSL. This acceleration contributed substantially to the formation and strengthening of a deep vortex.
4) The vortex intensified at low levels (0.5–2 km MSL) through vortex stretching. The outflow wind south of the vortex center accelerated to damaging strength. A weak and short-lived tornado was seen at the time when the diameter of the vortex reached a minimum.
5) A downdraft may have contributed to further sustainment and strengthening of the outflow wind and to the formation of microbursts.

This study benefited from a nearly optimal combination of various measuring systems. The availability of rapid radar volume scans was especially useful. The short time lag between the volume scans (2.5 min) allowed identification of some of the rapidly changing convective elements within this storm. To our knowledge, the formation of severe winds in weak-evolution storms has not been considered previously in numerical model simulations. We therefore believe that combining rapid-scan radar data of such storms and numerical model simulations can contribute to improve the understanding and the forecasting of storms of the type discussed in this study.

For nowcasting, it is important to note that severe winds in central Europe tend to be associated with secondary rapid cellular growth (Schmid et al. 1997). The timescale between the onset of cellular growth and the onset of damaging winds may be very short (some minutes). In such a setting, a successful nowcasting of severe winds has to be done on the basis of the precursor cell—cell 1 in the storm investigated here. In spite of the limited number of cases, we believe that storms of the type analyzed here and in Schmid et al. (1997) represent an important class of severe wind–producing storms in central Europe. Therefore, methods are sought that can help improve the prediction of the exact location and time of secondary cellular growth within an evolving thunderstorm.

Acknowledgments. Surface network data, radiosoundings, and radar data were obtained from the Swiss Meteorological Institute and from the WINDBANK project (PSI's Mesonetwork), which was implemented under the responsibility of Werner Graber. Volker Herrnberger from PSI provided the microbarograph data. Damage data were obtained from the forest agency (Kantonale Forstverwaltung Aargau) and the building insurance agency (Aargauisches Versicherungsamt). Willi Fuchs from MetAir provided aerial photographs that helped in the analysis of the damage. Wolfgang Linder operated the radar on 22 July 1995 and defined the correct sector-volume scans during the ''hot'' stage of the event. He and Susanne Mecklenburg developed computer programs for the analysis of the data, and David Bresch generously supported us in the use of the ARGOS soft-

ware. We also appreciate the helpful and constructive comments of two anonymous reviewers.

APPENDIX

Processing of the Doppler Radar Data

The properties of Doppler measurements depend on the characteristics of the radar, the Doppler processor, and on the software used to calculate and store the data. Doppler data need to be corrected and edited. An interactive procedure was written for this purpose, using the IDL graphics software package. Hereafter, we summarize the various steps in the process to obtain reliable Doppler data:

1) The PP02-Doppler processor (manufactured by Sigmet, Inc.) was programmed such that noisy Doppler velocities, caused by broad Doppler spectra, were set to ''missing data.'' The dual-PRF mode (e.g., Keeler and Passarelli 1990) was used to correct folded Doppler velocities in the interval -32 m s^{-1} . . . 32 m s^{-1}.
2) The Doppler data were stored in polar coordinates with a resolution of 0.5° in azimuth and 600 m in range. The PPI data were converted to a Cartesian grid before any other corrections were made. The ''nearest neighbor'' method was used for the conversion. Two data samples with different resolutions were produced (0.5 and 0.25 km), and the maximum ranges were restricted to 120 and 60 km, respectively. The motivation for this split was to minimize the size of the data samples and the computing time. On the other hand, a good spatial resolution was desired to minimize the loss of information by the coordinate conversion. The low-resolution sample was used when data beyond 60 km were needed (Figs. 11–13). Otherwise, we used the high-resolution data (Figs. 7, 14, and 15).
3) Folded Doppler data beyond the interval -32 m s^{-1} . . . 32 m s^{-1} were corrected with an interactive computer procedure.
4) Erroneous pixel values, caused by the dual-PRF method, were corrected with a procedure similar to that used by Environment Canada (P. Joe 1998, personal communication).
5) The Doppler data were carefully inspected for sidelobe echoes and flare echoes (Wilson and Reum 1988). Pixels affected by such echoes were set to missing data.
6) Missing data were replaced by interpolated data using a standard interpolation procedure. Such an interpolation may smooth out significant shear features. Therefore, calculated shear may underestimate the true shear in some cases.
7) The data were interpolated to horizontal layers (CAPPIs). Linear interpolation was performed in vertical direction.
8) The reflectivity and Doppler velocity data were smoothed with a three-point median smoother to reduce the disturbing influence of extreme pixel values. Calculated data of azimuthal shear were smoothed with a seven-point median smoother since the shear data, estimated from the first derivative of Doppler velocity, are noisier than the original Doppler velocity data.

REFERENCES

Biggerstaff, M. I., and R. C. Barritt, 1996: Role of gust front circulations in long-track severe straight-line winds. Preprints, *18th Conf. on Severe Local Storms,* San Francisco, CA, Amer. Meteor. Soc., 504–508.

Bluestein, H. B., and J. H. Golden, 1993: A review of tornado observations. *The Tornado: Its Structure, Dynamics, Prediction, and Hazards, Geophys. Monogr.*, No. 79, Amer. Geophys. Union, 319–352.

Charba, J., 1974: Application of gravity current model to analysis of squall-line gust front. *Mon. Wea. Rev.*, **102,** 140–156.

Dowell, D. C., and H. B. Bluestein, 1997: The Arcadia, Oklahoma, storm of 17 May 1981: Analysis of a supercell during tornadogenesis. *Mon. Wea. Rev.,* **125,** 2562–2582.

Droegemeier, K. K., S. M. Lazarus, and R. Davies-Jones, 1993: The influence of helicity on numerically simulated convective storms. *Mon. Wea. Rev.,* **121,** 2005–2029.

Foote, G. B., and H. W. Frank, 1983: Case study of a hailstorm in Colorado. Part III: Airflow from triple-Doppler measurements. *J. Atmos. Sci.,* **40,** 686–707.

Forbes, G. S., and R. M. Wakimoto, 1983: A concentrated outbreak of tornadoes, downbursts and microbursts, and implications regarding vortex classification. *Mon. Wea. Rev.,* **111,** 220–235.

Fovell, R. G., and Y. Ogura, 1988: Numerical simulation of a midlatitude squall line in two dimensions. *J. Atmos. Sci.,* **45,** 3846–3879.

——, and P. S. Dailey, 1995: The temporal behavior of numerically simulated multicell-type storms. Part I: Modes of behavior. *J. Atmos. Sci.,* **52,** 2073–2095.

Fujita, T. T., 1978: Manual of downburst identification for Project Nimrod. Satellite and Mesometeorology Research Paper No. 156, 104 pp. [Available from Department of Geophysical Sciences, University of Chicago, Chicago, IL 60637.]

——, 1981: Tornadoes and downbursts in the context of generalized planetary scales. *J. Atmos. Sci.,* **38,** 1511–1534.

——, 1985: The downburst. SMRP Research Paper No. 210, 122 pp. [Available from University of Chicago, Chicago, IL 60637.]

Funk, T. W., K. E. Darmofal, J. D. Kirkpatrick, M. T. Shields, R. W. Przybylinski, Y. J. Lin, G. K. Schmocker, and T. J. Shea, 1996a: Storm reflectivity and mesocyclone evolution associated with the 15 April 1994 derecho. Part II: Storm structure and evolution over Kentucky and southern Indiana. Preprints, *18th Conf. on Severe Local Storms,* San Francisco, CA, Amer. Meteor. Soc., 516–520.

——, B. F. Smull, and J. D. Amman, 1996b: Structure and evolution of an intense bow echo embedded within a heavy rain producing MCS over Missouri. Preprints, *18th Conf. on Severe Local Storms,* San Francisco, CA, Amer. Meteor. Soc., 521–526.

Furger, M., M. Jenni, and W. Schmid, 1996: The severe storm of 22 July 1995 in northern Switzerland—A tornado case study? *24th Int. Conf. on Alpine Meteorology (ICAM 96),* Bled, Slovenia, Hydrometeorological Institute of Slovenia, 153–159.

Hashem, M. S., and M. Biggerstaff, 1997: Organization of convection in mesoscale systems. Preprints, *28th Conf. on Radar Meteorology,* Austin, TX, Amer. Meteor. Soc., 483–484.

Houze, R. A., Jr., B. F. Smull, and P. Dodge, 1990: Mesoscale organization of springtime rain-storms in Oklahoma. *Mon. Wea. Rev.,* **118,** 613–654.

——, W. Schmid, R. G. Fovell, and H.-H. Schiesser, 1993: Hailstorms

in Switzerland: Left movers, right movers, and false hooks. *Mon. Wea. Rev.,* **121,** 3345–3370.

Jenni, M., 1997: Der Sturm über dem Fricktal vom 22. Juli 1995. M.S. thesis, Department of Geography, University of Bern, 107 pp. [Available from Institute of Geography, KLIMET, Hallerstrasse 12, CH-3012 Bern, Switzerland.]

Johnson, R. H., and P. J. Hamilton, 1988: The relationship of surface pressure features to the precipitation and airflow structure of an intense midlatitude squall line. *Mon. Wea. Rev.,* **116,** 1444–1472.

Keeler, R. J., and R. E. Passarelli, 1990: Signal processing for atmospheric radars. *Radar in Meteorology,* D. Atlas, Ed., Amer. Meteor. Soc., 199–229.

Kessinger, C. J., D. B. Parsons, and J. W. Wilson, 1988: Observations of a storm containing misocyclones, downbursts, and horizontal vortex circulations. *Mon. Wea. Rev.,* **116,** 1959–1982.

Klemp, J. B., 1987: Dynamics of tornadic thunderstorms. *Annu. Rev. Fluid Mech.,* **19,** 369–402.

Lee, W.-C., R. M. Wakimoto, and R. E. Carbone, 1992: The evolution and structure of a ''bow-echo–microburst'' event. Part II: The bow echo. *Mon. Wea. Rev.,* **120,** 2211–2225.

Lemon, L. R., and C. A. Doswell, 1979: Severe thunderstorm evolution and mesocyclone structure as related to tornadogenesis. *Mon. Wea. Rev.,* **107,** 1184–1197.

LeMone, M. A., 1983: Momentum transport by a line of cumulonimbus. *J. Atmos. Sci.,* **40,** 1815–1834.

Li, L., W. Schmid, and J. Joss, 1995: Nowcasting of motion and growth of precipitation with radar over a complex orography. *J. Appl. Meteor.,* **34,** 1286–1300.

Martin, F., R. Riosalido, and L. de Esteban, 1997: The Sigüenza tornado: A case study based on convective ingredients concept and conceptual models. *Meteor. Appl.,* **4,** 191–206.

Przybylinski, R. W., 1995: The bow-echo: Observations, numerical simulations and severe weather detection methods. *Wea. Forecasting,* **10,** 208–218.

Roberts, R. D., and J. W. Wilson, 1995: The genesis of three nonsupercell tornadoes observed with dual-Doppler radar. *Mon. Wea. Rev.,* **123,** 3408–3436.

Schiesser, H.-H., R. A. Houze Jr., and H. Huntrieser, 1995: The mesoscale structure of severe precipitation systems in Switzerland. *Mon. Wea. Rev.,* **123,** 2070–2097.

——, W. Schmid, R. A. Houze Jr., and B. Bauer-Messmer, 1996: A tornado-producing mesoscale convective system in northern Switzerland. Preprints, *Seventh Conf. on Mesoscale Processes,* Reading, United Kingdom, Amer. Meteor. Soc., 459–461.

Schmid, W., H.-H. Schiesser, and B. Bauer-Messmer, 1997: Supercell storms in Switzerland: Case studies and implications for nowcasting severe winds with Doppler radar. *Meteor. Appl.,* **4,** 49–67.

Schmocker, G. K., R. W. Przybilinski, and Y.-J. Lin, 1996: Forecasting the initial onset of damaging downburst winds associated with a mesoscale convective system (MCS) using the mid-altitude radial convergence (MARC) signature. Preprints, *15th Conf. on Weather Analysis and Forecasting,* Norfolk, VA, Amer. Meteor. Soc., 306–311.

Siggia, A. D., 1991: One pass velocity unfolding for VVP analysis. Preprints, *25th Conf. on Radar Meteorology,* Paris, France, Amer. Meteor. Soc., 882–884.

Smull, B. F., and R. A. Houze Jr., 1985: A midlatitude squall line with a trailing region of stratiform rain: Radar and satellite observations. *Mon. Wea. Rev.,* **113,** 117–133.

——, and ——, 1987: Rear inflow in squall lines with trailing stratiform precipitation. *Mon. Wea. Rev.,* **115,** 2869–2889.

Stensrud, D. J., J. V. Cortinas Jr., and H. E. Brooks, 1997: Discriminating between tornadic and nontornadic thunderstorms using mesoscale model output. *Wea. Forecasting,* **12,** 613–632.

Szoke, E. J., M. L. Weisman, J. M. Brown, F. Caracena, and T. W. Schlatter, 1984: A subsynoptic analysis of the Denver tornado of 3 June 1981. *Mon. Wea. Rev.,* **112,** 790–808.

Vasiloff, S. V., 1993: Single-Doppler radar study of a variety of tornado types. *The Tornado: Its Structure, Dynamics, Prediction, and Hazards, Geophys. Monogr.,* No. 79, Amer. Geophys. Union, 223–231.

Wakimoto, R. M., and J. W. Wilson, 1989: Non-supercell tornadoes. *Mon. Wea. Rev.,* **117,** 1113–1140.

——, and N. T. Atkins, 1996: Observations of the origins of rotation: The Newcastle tornado during VORTEX 94. *Mon. Wea. Rev.,* **124,** 384–407.

Waldteufel, P., and H. Corbin, 1979: On the analysis of single-Doppler radar data. *J. Appl. Meteor.,* **18,** 532–542.

Weisman, M. L., 1993: The genesis of severe, long-lived bow echoes. *J. Atmos. Sci.,* **50,** 645–670.

——, and J. B. Klemp, 1984: The structure and classification of numerically simulated convective storms in directionally varying wind shears. *Mon. Wea. Rev.,* **112,** 2479–2498.

Wicker, L. J., and R. B. Wilhelmson, 1995: Simulation and analysis of tornado development and decay within a three-dimensional supercell thunderstorm. *J. Atmos., Sci.,* **52,** 2675–2703.

Wilson, J. W., and D. Reum, 1988: The flare echo: Reflectivity and velocity signature. *J. Atmos. Oceanic Technol.,* **5,** 197–205.